Magneto-optical investigation of spin–orbit torques in metallic and insulating magnetic heterostructures

Mohammad Montazeri[1,*], Pramey Upadhyaya[1,*], Mehmet C. Onbasli[2], Guoqiang Yu[1], Kin L. Wong[1], Murong Lang[1], Yabin Fan[1], Xiang Li[1], Pedram Khalili Amiri[1], Robert N. Schwartz[1], Caroline A. Ross[2] & Kang L. Wang[1]

Manipulating magnetism by electric current is of great interest for both fundamental and technological reasons. Much effort has been dedicated to spin–orbit torques (SOTs) in metallic structures, while quantitative investigation of analogous phenomena in magnetic insulators remains challenging due to their low electrical conductivity. Here we address this challenge by exploiting the interaction of light with magnetic order, to directly measure SOTs in both metallic and insulating structures. The equivalency of optical and transport measurements is established by investigating a heavy-metal/ferromagnetic-metal device (Ta/CoFeB/MgO). Subsequently, SOTs are measured optically in the contrasting case of a magnetic-insulator/heavy-metal (YIG/Pt) heterostructure, where analogous transport measurements are not viable. We observe a large anti-damping torque in the YIG/Pt system, revealing its promise for spintronic device applications. Moreover, our results demonstrate that SOT physics is directly accessible by optical means in a range of materials, where transport measurements may not be possible.

[1] Department of Electrical Engineering, Device Research Laboratory, University of California, Los Angeles, California 90095, USA. [2] Departmentof Material Science and Engineering, Massachusetts Institute of Technology, Cambridge, Massachusetts 02139, USA. * These authors contributed equally to this work. Correspondence and requests for materials should be addressed to M.M. (email: mohammad.montazeri@gmail.com) or to K.L.W. (email: wang@seas.ucla.edu).

Current-induced manipulation of magnetic order through spin–orbit torques (SOTs) has attracted much attention, with the potential of enabling novel spintronic devices for memory and logic applications[1–14]. Specifically, metallic magnets incorporating high spin–orbit elements have been used to realize magnetic memory devices with fast switching and ultralow power consumption[6,8–10]. Beyond metallic structures, interests in magnetic insulators and controlling their dynamics by SOTs have been rising due to the inherently zero charge current and low energy dissipation of these materials[15–24].

To date, current-induced SOT physics is predominantly studied via electrical transport measurements. In metallic magnets, spin–orbit effects have been measured using both (i) direct measurement of current-induced magnetization dynamics[4,9,10,25], utilizing the non-zero electrical conductivity and the presence of magnetoresistance/anomalous-Hall (AH) effects; and (ii) its Onsager reciprocal process of dynamic magnetization-induced spin/charge pumping[5,8,13,26]. On the other hand, although the reciprocal spin pumping has been observed in insulators[15,27–30], with virtually zero conductivity, the direct quantitative electrical measurement of SOTs in such materials has proven a challenging task[21,31–33].

Light interacts with the magnetic order of both metallic and insulating materials through the magneto-optical (MO) Kerr effect. In particular, the linear and nonlinear dynamics of the magnetization in virtually any direction, and with high spatial and time resolution, can be studied by employing various microscopy and sub-picosecond pump–probe techniques[34–41]. To date, however, very limited efforts, specifically only on selected metallic structures, have been performed to partially incorporate the strength of MO measurements for investigating current-induced dynamics in magnetic heterostructures[42–44]. In particular, the nonlinear MO response of SOT has not been utilized in previous works.

Here we exploit MO measurements to directly probe the spin–orbit fields (SOFs) in two contrasting material systems, one a metallic thin film stack and the other an insulating magnetic heterostructure. The equivalency of MO and transport measurements is established by investigating SOFs of a micrometre-size ultra-thin Ta/CoFeB/MgO device wherein an excellent agreement between the optical and transport methods is found. In contrast to the metallic structures, the SOFs of a 50-nm-thick magnetic insulator yttrium iron garnet (YIG; $Y_3Fe_5O_{12}$), in contact with 4-nm-thick Pt, are then directly measured by optical means wherein analogous transport measurements on YIG/Pt are shown to be dominated by other phenomena such as spin-Seebeck effect. Unlike the perpendicular magnetization of the metallic stack, the YIG/Pt structure exhibits in-plane (IP) magnetization. Moreover, we find that both current-induced IP and out-of-plane (OOP) low-frequency oscillations of the magnetization are optically accessible through nonlinear MO terms, and can be separated by tuning the polarization of the incident light. The revealed polarization response of SOTs is unique to the optical measurements, with no analogous counterpart in transport measurements. We quantify a relatively large anti-damping field with a magnitude of 2.89×10^{-7} Oe A^{-1} cm^2 in YIG/Pt, which suggests its potential for spintronic devices based on magnetic insulators. Our results provide a direct and quantitative measurement of SOTs in insulating systems.

Results

Experimental set-up and theoretical considerations. The experimental set-up is schematically shown in Fig. 1. In short, a linearly polarized laser beam is tightly focused at the centre of a $20\,\mu m \times 130\,\mu m$ Hall bar device. The measured laser spot is $\sim 1\,\mu m$, much smaller than the dimensions of the device. With an IP applied magnetic field, the magnetization at the laser spot is
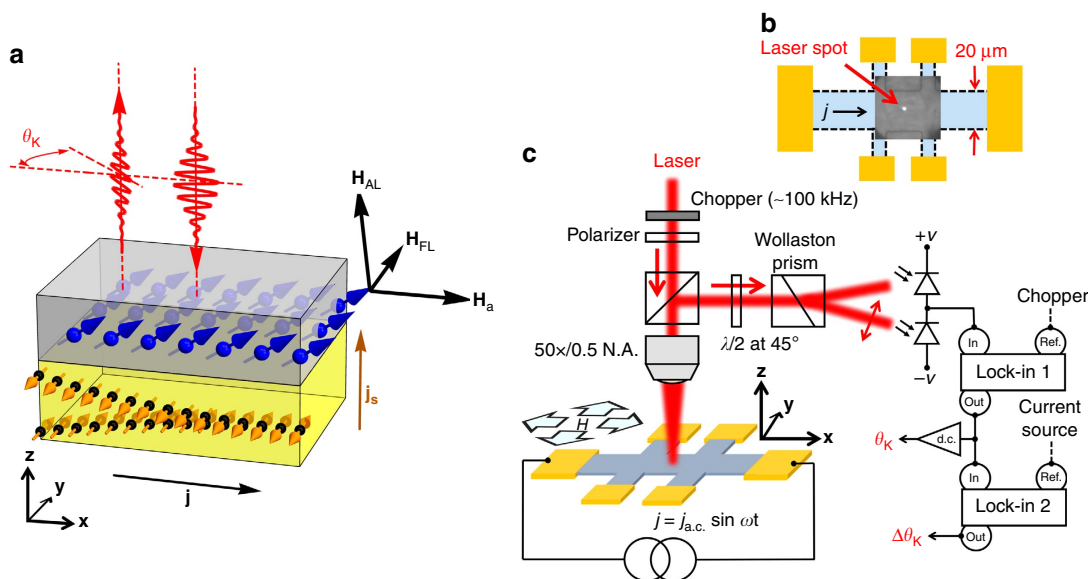
Figure 1 | MO probe of SOFs. (a) Schematic of the current-induced magnetization dynamics by SOFs, which is directly investigated for both metallic and insulating magnetic structures through the interaction of light with the magnetic order. The direction of applied and SOFs are shown by black arrows. H_a, H_{FL} and H_{AL} represent applied, field-like and anti-damping-like fields, respectively. Owing to spin–orbit interaction in heavy metal, a lateral current j produces a spin current j_s which propagates in perpendicular direction. **(b)** The optical microscope image of the central region of the device in which the laser (white spot) is tightly focused near the centre of the device. The laser spot size is measured at $\sim 1\,\mu m$, which is much smaller than the dimensions of the device, implying the imaging capabilities of the optical probe. **(c)** Schematic of the experimental set-up depicting the IP current and magnetic field and the backscattering geometry of the probe laser beam. A linearly polarized light is focused on the device using a microscope objective. The intensity of the light is modulated by a photoelastic modulator at 100 kHz. The polarization of the reflected beam is analysed using a half-wave plate at 45°, Wollaston prism and balanced photodiode. Two successive lock-in amplifiers are used to measure the Kerr rotation θ_K and the modulated Kerr signal $\Delta\theta_K$ induced by an IP a.c. current j with frequency of ~ 277 Hz while the external magnetic field is IP.

probed through the MO Kerr rotation (θ_K). The dynamics are induced through the SOTs via an IP a.c. current $j = j_{a.c.} \sin \omega t$ while, at the same time, the adiabatic current-induced change of the magnetization ($\Delta\theta_K$) at the laser spot is measured. In this backscattering geometry, the Kerr angle is linearly proportional to the OOP component of the magnetization, while the IP magnetization contributes through a second-order term, which is sensitive to the polarization of the incident light. Thus, θ_K is given by (Supplementary Note 1)

$$\theta_K = f_\perp m_z + f_\parallel m_l m_t \qquad (1)$$

where m_z is the OOP magnetization, m_l and m_t are longitudinal and transverse components of the IP magnetization with respect to the polarization of the light, and $f_\perp$ and $f_\parallel$ are the first- and second-order MO coefficients that parameterize the strength of the coupling of the light to the OOP and the IP magnetization[35,45–47].

The current-induced magnetization dynamics can be described by the Landau–Lifshitz–Gilbert equation given by

$$\partial_t \mathbf{m} = -\gamma \mathbf{m} \times \mathbf{H}_{eff} + \alpha \mathbf{m} \times \partial_t \mathbf{m} \qquad (2)$$

where $m = M/M_s$ is the magnetization unit vector normalized to the spontaneous magnetization M_s, γ is the gyromagnetic constant and α parameterizes the damping. The effective field H_{eff} is given by

$$\mathbf{H}_{eff} = \mathbf{H}_a + H_k \mathbf{m}_z + \mathbf{H}_{Oe} + \mathbf{H}_{FL} + \mathbf{H}_{AL} \qquad (3)$$

where $\mathbf{H}_a$ is the applied external magnetic field, H_k is the effective perpendicular anisotropy field and $\mathbf{H}_{Oe}$ is the current-induced Oersted field. The last two terms are the SOFs, namely field-like (FL) and anti-damping-like (AL) components, with $H_{FL} = \lambda_{FL} \mathbf{z} \times \mathbf{j}$ and $\mathbf{H}_{AL} = \lambda_{AL}(\mathbf{j} \times \mathbf{z}) \times \mathbf{m}$ (ref. 9). Here, $\mathbf{j}$ is the current density, $\mathbf{z}$ is the unit vector normal to the plane and λ's quantify the strength of the SOFs. Since the low-frequency-current-induced dynamics (with frequency of $\sim 10^3$ Hz) are orders of magnitude slower than the magnetization precession frequency ($\sim 10^9$ Hz), it is reasonable to assume that the magnetization adiabatically follows the $\mathbf{H}_{eff}$ and thus the quasi-equilibrium condition is described by $\mathbf{m} \times \mathbf{H}_{eff} = 0$. Furthermore, we treat the SOT-induced low-frequency oscillation of the magnetization as a perturbation on the equilibrium condition defined by $j = 0$.

SOFs in metallic Ta/CoFeB/MgO. To validate the optical probe, first we investigate an ultra-thin metallic stack of Ta(5 nm)/ $Co_{20}Fe_{60}B_{20}$(1.1 nm)/MgO(2.0 nm) with perpendicular magnetic anisotropy. The advantage of the metallic example is that the optical measurements can be directly compared and correlated with standard transport methods. The device is in a single domain state at the applied bias field and shows current-induced switching that is locally probed at the laser spot (Supplementary Note 2 and Supplementary Fig. 1).

With our geometry, the optical measurements on Ta/CoFeB/ MgO are dominantly sensitive to the change of the OOP component of the magnetization, with only a minor contribution from the IP oscillations. Figure 2a,b show θ_K ($\sim m_z$) and $\Delta\theta_K$ ($\sim \Delta m_z$) for the magnetic field parallel to the current density of 4.6×10^6 A cm^{-2}. At fields larger than H_k, the magnetization is aligned with the external field, which is evident by a nearly
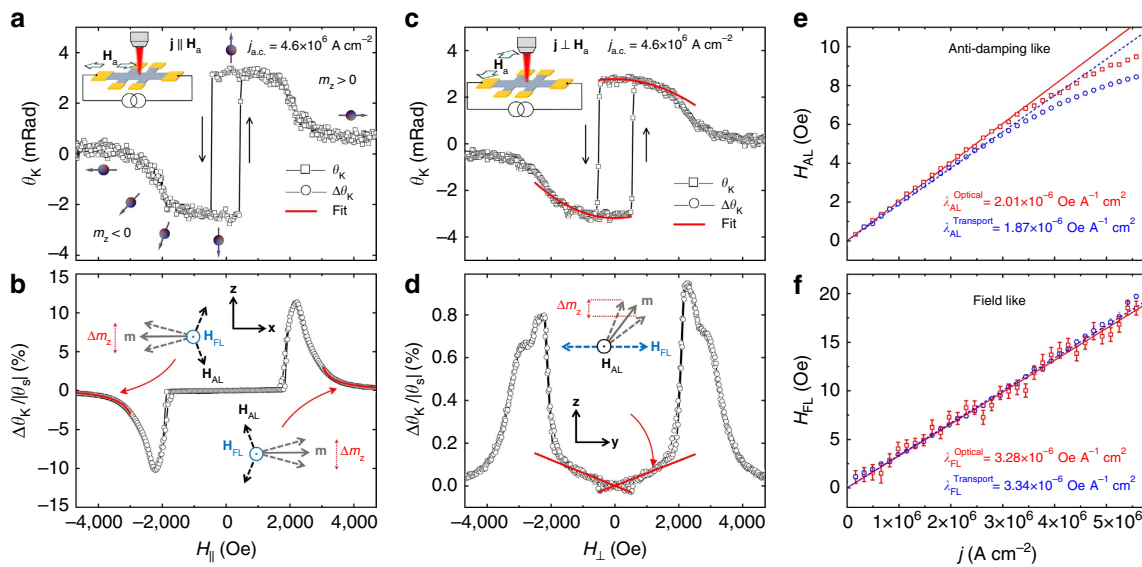
Figure 2 | Optical measurements of metallic Ta/CoFeB/MgO. Experimentally measured Kerr angle (θ_K) and (normalized) differential Kerr angle ($\Delta\theta_K$) for the magnetic field parallel (**a,b**) or perpendicular (**c,d**) to the current with current density of 4.6×10^6 A cm^{-2} and with $\theta_S = \theta_K(H_a = 0)$. The schematics in **a,b** show the direction of the magnetic field with respect to the current. The arrow balls in **a** schematically show the direction of the magnetic moment at various magnetic field. The θ_K and $\Delta\theta_K$ are proportional to m_z and Δm_z, respectively. The sharp edges in **a,c** indicate OOP switching of the magnetization due to a small OOP component of the external field. The asymmetric and symmetric line shapes in **b,d** reflect the symmetries of the anti-damping-like and field-like spin–orbit effective fields under magnetization reversal, respectively. The current-induced dynamics of magnetization **m** and relevant directions of SOFs are schematically demonstrated in **b,d**. For $\mathbf{j} \| \mathbf{H}_a$, the anti-damping field is quantified by fitting equation (4) to the experiment at large fields (solid red lines in **b**). For $\mathbf{j} \perp \mathbf{H}_a$, the field-like effective field is measured from the curvature of θ_K (solid red line in **c**) and the slope of $\Delta\theta_K$ (solid red line in **d**). Comparison of optical (red box) and transport (blue circle) measurements of anti-damping-like and field-like effective fields at various current densities for Ta/CoFeB/MgO is shown in **e,f**, respectively. In **e,f**, the solid red lines are linear fits to the optical probe, whereas the dashed blue lines are linear fits to the transport results. In **e**, the fits quantify the anti-damping-like coefficients λ_{AL} at $(2.01 \pm 0.01) \times 10^{-6}$ and $(1.87 \pm 0.01) \times 10^{-6}$ Oe A^{-1} cm^2 for optical and transport probes, respectively. In **f**, the field-like coefficients λ_{FL} for the optical and transport probes are measured at $(3.28 \pm 0.03) \times 10^{-6}$ and $(3.34 \pm 0.02) \times 10^{-6}$ Oe A^{-1} cm^2, respectively. The error bars in **e,f** are obtained by linear regression. The error bars in **e** are smaller than symbols. The consistency demonstrates the equivalency and relevance of the MO probe technique for investigating the SOTs in magnetic structures.
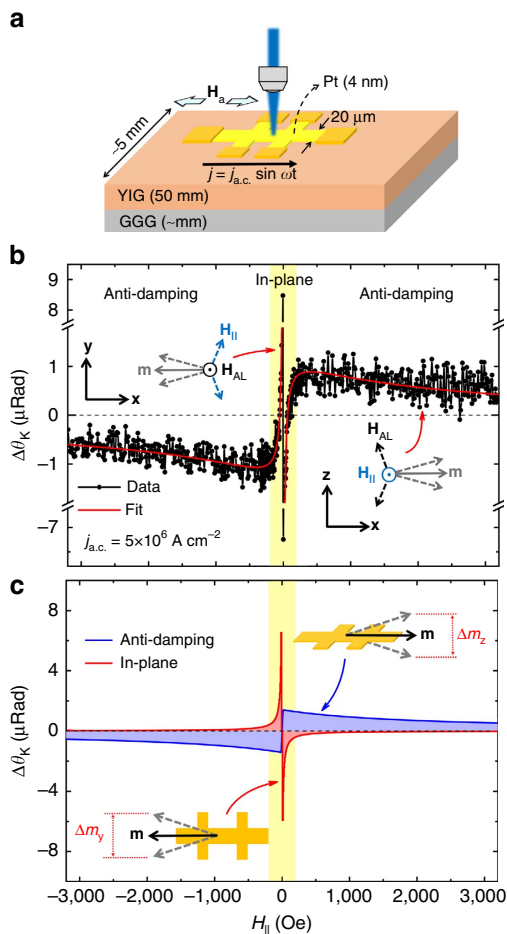
Figure 3 | Current-induced differential Kerr of YIG/Pt structure.
(**a**) The structure of the material in which a micrometre-size 4-nm-thick Pt device is fabricated on a mm-size 50-nm-thick insulating YIG substrate.
(**b**) The differential Kerr signal of YIG/Pt with the magnetic field and the polarization of the incident light parallel to the current. The horizontal dashed line marks $\Delta\theta_K = 0$. As demonstrated schematically in **b,c**, with this geometry, the anti-damping field drives the OOP low-frequency oscillation of the magnetization, whereas the field-like and Oersted fields drive the IP oscillation. The shaded area highlights the sharp diverging-like features at low fields corresponding to the IP oscillations partially driven by the field-like effective field. The broader component, most evident at higher fields, corresponds to the OOP oscillation driven by the anti-damping field. Equation (5) fits well to the experimental data (solid red line in **b**) where the individual contributions due to anti-damping and IP fields are shown in **c**.

constant $\theta_K \approx 0$. Thus, while H_{AL} induces OOP oscillations, H_{FL} drives the IP oscillations of the magnetization. The differential Kerr signal ($\Delta\theta_K$) is therefore dominantly driven by H_{AL} and is relatively insensitive to H_{FL}. The signal at large fields is proportional to the strength of H_{AL}, with a $1/(H_a - H_k)$ dependence indicating the oscillatory nature of $\Delta\theta_K$. At near-zero field, $\Delta\theta_K$ weakens significantly since the OOP magnetization results in a nearly zero net change of m_z at the first harmonic of the current. At fields larger than the anisotropy, H_{AL} can be quantified by (Supplementary Note 1)

$$\Delta\theta_K = \frac{H_{AL}f_\perp}{H_a - H_k} \quad (4)$$

where $f_\perp (= \theta_S)$ is readily available from θ_K at $H_a = 0$, resulting in $H_{AL} = 8.50 \pm 0.08$ Oe for this example. Similarly, H_{FL} can be

investigated by aligning H_a perpendicular to the current (Fig. 2c,d). In this case, at low fields, H_{FL} oscillates the magnetization in the y–z plane while the H_{AL} causes an IP oscillation, which does not contribute to $\Delta\theta_K$. For the current density of 4.6×10^6 A cm^{-2} shown in Fig. 2c,d, the FL effective field is measured at $H_{FL} = 14.9 \pm 0.7$ Oe (see Supplementary Note 3 for details).

The current dependence of H_{AL} and H_{FL} is summarized in Fig. 2e,f and are compared with the second-harmonic analysis of the AH voltage on the same device. The details of the transport measurements and comparisons are presented in Supplementary Note 3 and Supplementary Figs 2 and 3. For both optical and transport measurements shown in Fig. 2e, while the H_{AL} shows a linear dependence on the current densities up to $\sim 3.5 \times 10^6$ A cm^{-2}, at larger current a nonlinearity emerges that could be either due to Joule heating or deviation of the dynamics from the linear regime. Linear fits to the lower side of the data yields $\lambda_{AL}^{Optical} = (2.01 \pm 0.01) \times 10^{-6}$ Oe A^{-1} cm^2 and $\lambda_{AL}^{Transport} = (1.87 \pm 0.01) \times 10^{-6}$ Oe A^{-1}cm^2 for the optical and transport measurements, respectively. These values, both the magnitudes and the signs, are in agreement with that reported in the literature for a similar structure[9]. The optically measured λ_{AL} is $\sim 7\%$ larger than that of the transport measurement, which may be due to the contribution of the planar-Hall effect and/or other nonlinear terms to the AH resistance in the transport or higher-order terms in the optical measurements. The measured FL coefficients are $\lambda_{FL}^{Optical} = (3.28 \pm 0.03) \times 10^{-6}$ Oe A^{-1} cm^2 and $\lambda_{FL}^{Transport} = (3.34 \pm 0.02) \times 10^{-6}$ Oe A^{-1} cm^2, consistent with a previous report[9].

To summarize this part, the consistency of the MO and transport measurements of SOFs in metallic Ta/CoFeB/MgO establishes both the equivalency and the relevance of the optical probe for investigating SOT-related phenomena.

SOTs in insulating YIG/Pt. Light interacts with the magnetic order of both metallic and insulating magnetic materials. To this end, we use the MO probe to examine a prototypical magnetic-insulator/heavy-metal structure in which the magnetization of the insulator (YIG) is modulated by an IP current through the heavy metal (Pt). As shown in Fig. 3a, the structure consists of micrometre-size 4-nm-thick Pt Hall bar device on a mm-size 50-nm-thick YIG film grown on a gadolinium gallium garnet (GGG) substrate (see Methods, Supplementary Note 4, Supplementary Fig. 4 and refs 23,48 for more details on YIG). Furthermore, the YIG exhibits an IP magnetization in contrast to the OOP magnetization of Ta/CoFeB/MgO. The details of the measurements are similar to the metallic case. Owing to the IP magnetization, the θ_K remains constant (zero), whereas a pronounced current-induced $\Delta\theta_K$ is observed. An example of $\Delta\theta_K$ with the current density $j_{a.c.} = 5 \times 10^6$ A cm^{-2} is shown in Fig. 3b, wherein both the current and the polarization of the laser are parallel to the magnetic field. Interestingly, $\Delta\theta_K$ behaves very differently compared with the metallic case. Moreover, two distinct regimes are identified: a sharp diverging-like feature at lower fields and a broader, slow-decaying component most evident at the higher fields. With this geometry, H_{AL} and H_{FL} point along the OOP and IP directions, respectively. Thus, the differential Kerr signal induced by the current parallel to the magnetic field reads (Supplementary Note 1)

$$\Delta\theta_K = f_\perp \Delta m_z + f_\parallel \Delta(m_l m_t) = \frac{f_\perp H_{AL}}{H_a - H_k} + \frac{f_\parallel h_\parallel \cos 2\phi_P}{H_a} \quad (5)$$

where $H_k < 0$ (unlike $H_k > 0$ in Ta/CoFeB/MgO), ϕ_P is the angle between the current and the polarization of the laser, and $h_\parallel = H_{FL} + H_{Oe}$. Both H_{AL} and H_{FL} contribute to $\Delta\theta_K$.
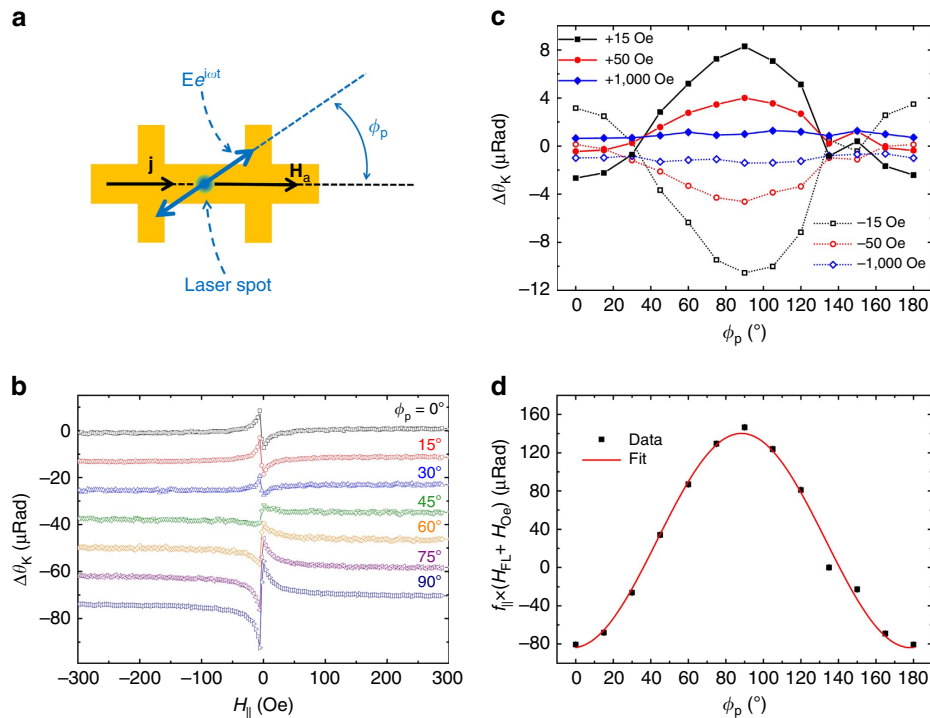
Figure 4 | Polarization dependence of the differential Kerr of YIG/Pt. (a) Schematic of the measurements in which the IP magnetic field is parallel to the current and the polarization of the perpendicularly incident light (ϕ_p) is varied with respect to the field. **(b)** Comparison of the differential Kerr signal of YIG/Pt at lower fields for different polarizations of the light. **(c)** Polarization dependence of $\Delta\theta_K$ at various external fields. While the differential Kerr signal shows a sinusoidal dependence at low fields, it is insensitive to the polarization at higher fields. **(d)** Amplitude of $\Delta\theta_K$ due to IP oscillations extracted from a theoretical fit of equation (5) to the experiment. The solid line in **d** is a theoretical fit to $\cos 2\phi_p$. The contribution of the IP oscillation to $\Delta\theta_K$ vanishes at $\phi_p \approx 40°$.

Furthermore, the low-frequency OOP oscillation is induced by H_{AL} and competes against the H_k with a $1/(H_a - H_k)$ dependence, while the free IP oscillation is partly driven by H_{FL} and diverges at $H_a = 0$. Comparing with the experimental data in Fig. 3b, we find that the diverging-like and the slow-decaying components are associated with the current-induced IP and OOP oscillations, respectively. The experimental data fit very well to equation (5) using the individual contributions of the IP and OOP oscillations that are reported in Fig. 3c.

It is noted that the differential Kerr of the IP oscillation is sensitive to the polarization of the incident light, whereas the AL component is insensitive to the polarization; as is verified experimentally. This polarization dependence is unique to the MO probe and has no analogous counterpart in transport measurements. Figure 4 summarizes the polarization dependence of $\Delta\theta_K$ at a given current density. The diverging-like component, corresponding to the IP reorientation, shows a strong polarization dependence with minimum and maximum amplitudes at $\phi_p = 0°$ and $90°$, respectively. On the other hand, the $\Delta\theta_K$ at higher fields, corresponding to the H_{AL}-induced OOP oscillations, shows no obvious polarization dependence as illustrated in Fig. 4c. The relative amplitude of the $h_{||}$ versus polarization is extracted from a theoretical fit of equation (5) to the experimental data in Fig. 4b and is plotted in Fig. 4d. The data fit well to $\cos 2\phi_p$ as predicted by equation (5). The small shift in vertical direction might be due to possible IP anisotropy or higher-order effects that are ignored here. These observations strongly support the attribution of the OOP and IP oscillations to the slow-decaying and the diverging-like components of $\Delta\theta_K$, respectively. Although in principle it is possible to extract the value of the H_{FL}, here however we expect that the H_{Oe} dominates the IP oscillation (Supplementary Note 5 and Supplementary Fig. 5). Furthermore, it is noted that the

contribution of the IP oscillation is completely suppressed at $\phi_p \approx 40°$ and thus, at this polarization the signal is dominantly induced by the anti-damping field.

In a sharp contrast to the metallic case, the harmonic analysis of the transverse-Hall magnetoresistance of YIG/Pt[19,32,49,50] system is significantly dominated by other nonlinear effects, for example, the spin-Seebeck effect[51]. To demonstrate this, it is instructive to define a dimensionless quantity η that relates the MO and transport measurements to the magnetization dynamics through the identity

$$\eta = \frac{\Delta m_z}{m_S} = \frac{\Delta\theta_K}{f_\perp} = \frac{2R_{xy}^{2f}}{r_\perp} \qquad (6)$$

where R_{xy}^{2f} is the second-harmonic transverse-Hall resistance $R_{xy} = r_\perp m_z + r_{||} m_x m_y$ where the coefficients $r_\perp$ and $r_{||}$ depend on intrinsic material properties (refs 18,51, Supplementary Note 6 and Supplementary Fig. 6). Noting that the identity (equation (6)) is also valid for the anomalous Hall (AH) effect (Supplementary Note 3), Fig. 5a,b compares η_{MO} and η_{AH} for Ta/CoFeB/MgO with the OOP and IP anisotropy ($H_k > 0$ and $H_k < 0$, respectively) wherein the values of η_{MO} and η_{AH} are extracted from either MO or AH measurements, respectively. The coefficients $r_\perp$ and $f_\perp$ for the IP Ta/CoFeB/MgO are separately measured by applying magnetic field normal to the plane and are demonstrated in Fig. 5c. Note here that the current is parallel to H_a resulting in the dominant contribution of the H_{AL}. In both cases, the identity in equation (6) is verified, which indicates that both the optical and transport signals in Ta/CoFeB/MgO originate in the SOT, regardless of the sign of H_k. In sharp contrast, for the YIG/Pt device the identity (equation (6)) is violated showing $\eta_{MR} \gg \eta_{MO}$, as illustrated in Fig. 5d, where η_{MO} is expanded by $1,000 \times$ for
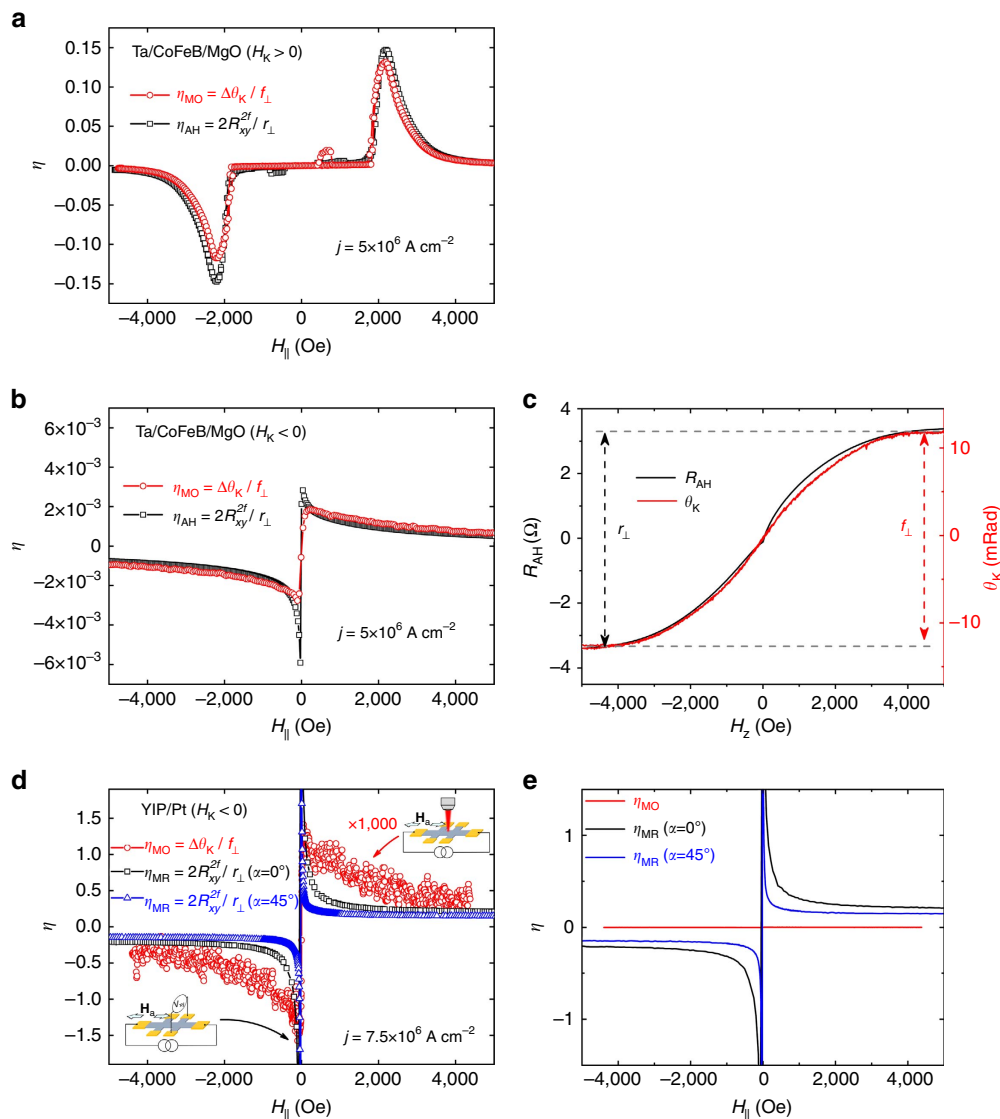
Figure 5 | Comparison of MO and transport measurements. Comparison of $\eta_{MO} = \Delta\theta_K/f_\perp$ from MO (red circles) and $\eta_{AH/MR} = \Delta R_{xy}^{2f}/r_\perp$ from second-harmonic anomalous-Hall/transverse-Hall (black boxes) measurements for **a** metallic Ta/CoFeB/MgO with OOP anisotropy ($H_k > 0$), (**b**) Ta/CoFeB/MgO with IP anisotropy ($H_k < 0$) and (**d**) insulating YIG/Pt. In **a**, $f_\perp$ and $r_\perp$ are readily available from MOKE/AH measurements. For IP Ta/CoFeB/MgO in **b,c** shows MOKE and AH measurements with OOP field to extract $f_\perp$ and $r_\perp$, respectively. In **a,b** the current is parallel to the field while in **c** η_{MR} is demonstrated for both current being parallel (black boxes) and at 45° to the field (blue triangles) corresponding to $\alpha = 0°$ and 45°, respectively. In **d** η_{MO} is expanded by ×1,000 for clarity while the direct comparison of η's is shown in **e**. Equation (6) is validated for Ta/CoFeB/MgO regardless of the sign of the anisotropy as shown in **a,b** demonstrating that both optical and transport signals in Ta/CoFeB/MgO originate in SOT. In a sharp contrast the equation (6) is violated for YIG/Pt system as demonstrated in **d,e**. In YIG/Pt, the contribution of SOT in transport measurements is significantly overwhelmed by other nonlinear effects (for example, spin-Seebeck effect) resulting in $\eta_{MR} \gg \eta_{MO}$ as illustrated in **d**. This comparison demonstrates the superiority of MO measurements for studying SOTs in insulating systems.

clarity while a direct comparison is presented in Fig. 5e. The measured $r_\perp$ and $f_\perp$ that are used to obtain η's for the YIG/Pt device are presented in Supplementary Notes 6 and 7 and Supplementary Fig. 6. In Fig. 5d,e, η_{MR} of YIG/Pt is demonstrated for both the current direction being parallel and at 45° to the field ($\alpha = 0°$ and 45°, respectively). Thus the contribution of $h_\parallel$ is minimized for η_{MR} with $\alpha = 45°$ as well as η_{MO} (Supplementary Note 6). Furthermore, the η's exhibit different field dependences: while η_{MO} approaches zero with a $1/(H_a - H_k)$ dependence, η_{MR} remains finite at large fields (even up to 1 T). In addition, with $\alpha = 45°$, the presence of the diverging-like signal is not consistent with current-induced IP reorientation (Supplementary Note 6 and Supplementary Fig. 7). These observations strongly suggest

that the contribution of H_{AL} to the transverse-Hall signal is significantly overwhelmed by other nonlinear effects such as the spin-Seebeck effect (Supplementary Note 6, Supplementary Fig. 8 and ref. 51) and thus may not provide a clean nor direct measurement of the SOTs. It is noted that such nonlinear effects do not contribute to the optical measurements since $\Delta\theta_K \propto j$ while the measured second-harmonic transverse voltage $V_{xy}^{2f} \propto j^2$.

We report the current dependence of $\Delta\theta_K$ of YIG/Pt in Fig. 6 with the polarization set to $\phi_p = 40°$ for which only H_{AL} makes a contribution. The data fit very well to the first term of equation (6) providing a quantitative measure of the H_{AL}. The coefficient $f_\perp$ in equation (6) is independently measured (Supplementary Note 7 and Supplementary Fig. 9). Figure 6b
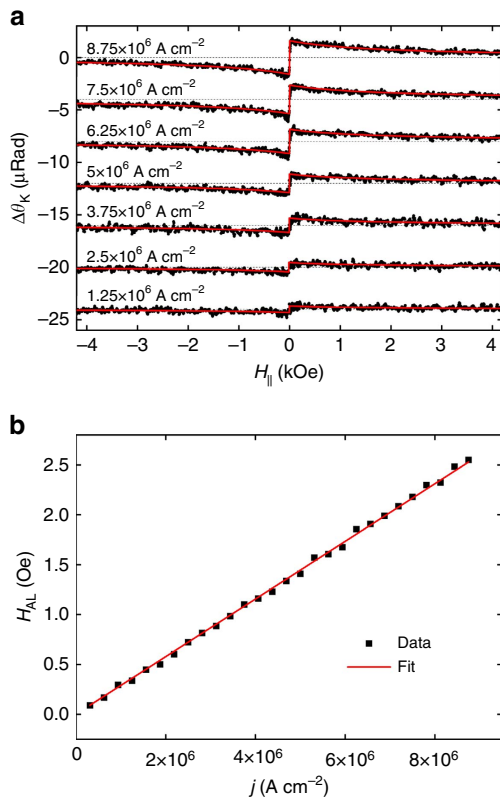
Figure 6 | Optically measured anti-damping field of YIG/Pt. (**a**) Current dependence of the differential Kerr signal of YIG/Pt device with the polarization of the light set to $\phi_p \approx 40°$ to minimize the contribution of the IP oscillation. Solid red lines in **a** are theoretical fits of the anti-damping-induced component of equation (6) to the experimental data. Dashed lines in **a** mark $\Delta\theta_K = 0$. (**b**) The measured anti-damping field in YIG/Pt versus the current density through the Pt device. The error bars in **b** (obtained by linear regression) are smaller than the symbols. The solid red line in **b** is a linear fit to the data that yields the anti-damping coefficient $\lambda_{AL} = (2.89 \pm 0.02) \times 10^{-7}$ Oe A^{-1} cm^2.

shows H_{AL} at various current densities demonstrating a linear dependence resulting in $\lambda_{AL} = (2.89 \pm 0.02) \times 10^{-7}$ Oe A^{-1} cm^2 from a linear fit to the data.

Discussion

In our measurements, the sign of the λ_{AL} in YIG/Pt is similar to the positive sign obtained in Ta/CoFeB/MgO. However, in the YIG/Pt, the Pt is on the top of the magnetic structure, whereas in the Ta/CoFeB/MgO the heavy metal (Ta) is at the bottom side of the structure resulting in a sign reversal in each structure with respect to the other. Thus, the λ_{AL} in Pt has the opposite sign compared with Ta, which is consistent with their relative signs of the spin-Hall angle[52]. The magnitude of λ_{AL} in YIG/Pt is nearly one order of magnitude smaller than that observed for Ta/CoFeB/MgO. One should note however that the 50-nm-thick YIG is substantially thicker than the 1.1-nm-thick CoFeB. Furthermore, the spin transmission efficiency at the YIG/Pt interface could be as small as 0.15 (ref. 21). A more direct comparison can be obtained by noting that $\lambda_{AL} \sim T\theta_{SH}/(t_{FM}M_S)$; where θ_{SH} is the spin-Hall angle of the heavy metal, t_{FM} is the thickness of the magnetic layer and T characterizes the effective spin transmission at the interface of heavy metal and magnetic layer[21]. Using the experimentally measured λ_{AL}'s for YIG/Pt and Ta/CoFeB/MgO, we obtain $(T\theta_{SH})_{YIG/Pt}/(T\theta_{SH})_{Ta/CoFeB} = 0.69$. Here we used

values for M_s of 75 emu cm^{-3} and 700 emu cm^{-3} for YIG and CoFeB, respectively (Supplementary Note 4 and ref. 53). Overall, our data suggest that λ_{AL} in YIG/Pt is relatively large and can potentially be used to switch the magnetization by reducing the thickness and perhaps the lateral dimensions of the YIG, as well as using materials with higher spin-Hall angle such as topological insulators[25,48].

Because of the experimental limitations inherent in the transport techniques, very limited efforts have been reported to quantify the strength of the SOTs in YIG-based devices. As discussed earlier, the transverse-Hall magnetoresistance is significantly dominated by other nonlinear transport mechanisms such as the spin-Seebeck effect[51]. Magnetic resonance force microscopy has been employed to investigate the mechanical resonance of a magnetic cantilever dipole coupled to a micro-disk of YIG/Pt where a rate of 0.5 Oe mA$^{-1} \sim 1.7 \times 10^{-7}$ Oe A^{-1} cm^2 change in the linewidth, including inhomogeneous broadening, for 20-nm-thick YIG was reported[21]. Spin pumping at ferromagnetic resonance and spin-Hall magnetoresistance rectification has also recently been used to investigate a mm-size YIG/Pt structure where one can calculate an anti-damping field of 1.8–2.0 $\times 10^{-7}$ Oe A^{-1} cm^2 from the reported results for 55-nm-thick YIG[30]. However, the dominant contribution of the Oersted field and the complex line shape of the resonance signal demand thickness-dependent measurements along with extensive numerical simulations, which thus limits the quantitative measure of the magnitude of the SOT[54]. While our work suggest that spin-Seebeck and other possible nonlinear effects have a dominant contribution, it might be possible to account for these effects in all-electrical resonance measurements. The MO measurements, however, overcome these limitations and provide a superior direct and quantitative probe of the SOTs in virtually any magnetic-insulator structure with diffraction-limited spatial resolution, regardless of thickness and geometry.

In summary, we demonstrate that SOT physics of magnetic heterostructures are directly accessible and can be accurately measured by optical means, regardless of their electrical conductivity. The relevance of the MO probe is established by investigating a metallic Ta/CoFeB/MgO structure, and is then extended to an insulating YIG/Pt structure where the transport techniques are considerably limited. We reveal that in the optical probe, the polarization of the light also carries information on SOTs, whereas there is no analogous counterpart in transport measurements. Our specific result on YIG/Pt quantifies a relatively large anti-damping field of 2.89 $\times 10^{-7}$ Oe A^{-1} cm^2. Our work opens up exciting opportunities in revealing SOT physics, particularly for investigating the spin-transfer mechanisms and spin-wave physics in magnetic insulators as well as magnetization dynamics of devices with internal magnetic textures.

Methods

Ta/CoFeB/MgO. Material stacks consisting of Ta(5 nm)/Co$_{20}$Fe$_{60}$B$_{20}$(1.1 nm)/MgO(2.0 nm)/TaO$_x$ layers are sputter deposited at room temperature on a thermally oxidized Si/SiO$_2$ substrate. The 2 nm MgO is grown by rf-sputtering from an MgO insulator target. The TaO$_x$ layer is formed by oxidizing a 1.5-nm Ta layer under an O$_2$/Ar plasma for protection. The films are annealed to enhance the perpendicular magnetic anisotropy. Further details can be found in ref. 53.

YIG/Pt. Yttrium iron garnet (Y$_3$Fe$_5$O$_{12}$, YIG) films were grown on GGG (Gd$_3$Ga$_5$O$_{12}$) (111) substrates using pulsed laser deposition (see Supplementary Note 4 and refs 23,48 for details). The Pt layer of 4 nm thickness was deposited by d.c. magnetron sputtering at room temperature.

Device fabrication. The films are patterned into 20 × 130-μm Hall bar devices by standard photolithographic and dry etching techniques.

Optical measurements. The devices are mounted on a custom built XYZ translational stage and a linearly polarized laser beam is tightly focused on the device using a $50 \times /0.42$ NA (numerical aperture) long working-distance microscope objective. Special care was taken to assure the optical axis is normal to the plane of the sample with better than $1°$ accuracy, excluding the finite NA of the objective. The laser spot size is measured at $\sim 1\,\mu m$, which is much smaller than the $20\,\mu m$ width and $130\,\mu m$ length of the device and is placed at the centre of the device, both in the lateral and longitudinal directions. At the lateral centre of the device the normal component of the Oersted field vanishes and thus m_z is not directly modulated by the Oersted field. At the maximum current density used in our measurements, the IP component of the Oersted field is estimated at < 2 Oe. The back-reflected light is collected by the same microscope objective and rotation of the polarization plane is analysed using a Wollaston prism and a balanced silicon photodetector. To improve the signal-to-noise ratio, the intensity of the laser was modulated at $\sim 100\,kHz$ using a combination of a photoelastic modulator and a linear polarizer. To modulate the magnetization through SOTs, an a.c. current of $j = j_{a.c.} \sin \omega t$ with frequency of ~ 277 Hz, variable amplitude and zero d.c. offset is used. Two successive lock-in amplifiers were employed to analyse the output signal of the balanced photodetector. While the first lock-in (time constant of $100\,\mu s$), locked to the frequency of the photoelastic modulator, measures the relative magnitude of the Kerr angle θ_K, the second lock-in (time constant of 300 ms) is locked to the frequency of the current source and probes any change in the Kerr angle induced by the current ($\Delta \theta_K$). It should be noted that nonlinear components in $\Delta \theta_K$, such as heating, may appear at higher harmonics and thus makes a minor contribution to our first-harmonic measurements. The external magnetic field is kept IP with some small OOP component ($< 2°$) such that $m_z > 0$ for positive IP fields. The presented data for Ta/CoFeB/MgO are obtained by employing a 80 MHz mode-locked Ti:Sapphire laser centred at 840 nm. The same results are reproduced by 632.8- and 730-nm CW lasers. For YIG/Pt structure, to improve the transmission of the laser through the Pt, a laser beam of 420 nm is employed, which was generated through second-harmonic generation by a beta barium borate crystal pumped by a 840-nm mode-locked laser. This significantly improved the signal-to-noise ratio compared with 840-nm mode-locked or CW lasers. For both Ta/CoFeB/MgO and YIG/Pt, the signal is linearly proportional to the intensity of the laser with no obvious laser-induced heating effects. The presented data are for a laser average intensity of $\sim 20\,\mu W\,cm^{-2}$ for both the metallic and insulating cases. Measurements are performed at ambient condition.

Transport measurements. Transport measurements are performed immediately after the optical measurement without altering the geometry and with the laser beam being blocked.

References

1. Ando, K. *et al.* Electric manipulation of spin relaxation using the spin Hall effect. *Phys. Rev. Lett.* **101,** 036601 (2008).
2. Mihai Miron, I. *et al.* Current-driven spin torque induced by the Rashba effect in a ferromagnetic metal layer. *Nat. Mater.* **9,** 230–234 (2010).
3. Miron, I. M. *et al.* Perpendicular switching of a single ferromagnetic layer induced by in-plane current injection. *Nature* **476,** 189–193 (2011).
4. Pi, U. H. *et al.* Tilting of the spin orientation induced by Rashba effect in ferromagnetic metal layer. *Appl. Phys. Lett.* **97,** 162507 (2010).
5. Liu, L., Moriyama, T., Ralph, D. C. & Buhrman, R. A. Spin-torque ferromagnetic resonance induced by the spin Hall effect. *Phys. Rev. Lett.* **106,** 036601 (2011).
6. Liu, L., Lee, O. J., Gudmundsen, T. J., Ralph, D. C. & Buhrman, R. A. Current-induced switching of perpendicularly magnetized magnetic layers using spin torque from the spin Hall effect. *Phys. Rev. Lett.* **109,** 096602 (2012).
7. Pai, C.-F. *et al.* Spin transfer torque devices utilizing the giant spin Hall effect of tungsten. *Appl. Phys. Lett.* **101,** 122404 (2012).
8. Liu, L. *et al.* Spin-torque switching with the giant spin Hall effect of tantalum. *Science* **336,** 555–558 (2012).
9. Garello, K. *et al.* Symmetry and magnitude of spin-orbit torques in ferromagnetic heterostructures. *Nat. Nanotechnol.* **8,** 587–593 (2013).
10. Kim, J. *et al.* Layer thickness dependence of the current-induced effective field vector in Ta|CoFeB|MgO. *Nat. Mater.* **12,** 240–245 (2013).
11. Ryu, K.-S., Thomas, L., Yang, S.-H. & Parkin, S. Chiral spin torque at magnetic domain walls. *Nat. Nanotechnol.* **8,** 527–533 (2013).
12. Emori, S., Bauer, U., Ahn, S.-M., Martinez, E. & Beach, G. S. D. Current-driven dynamics of chiral ferromagnetic domain walls. *Nat. Mater.* **12,** 611–616 (2013).
13. Mellnik, A. R. *et al.* Spin-transfer torque generated by a topological insulator. *Nature* **511,** 449–451 (2014).
14. Yu, G. *et al.* Switching of perpendicular magnetization by spin-orbit torques in the absence of external magnetic fields. *Nat. Nanotechnol.* **9,** 548–554 (2014).
15. Kajiwara, Y. *et al.* Transmission of electrical signals by spin-wave interconversion in a magnetic insulator. *Nature* **464,** 262–266 (2010).
16. Uchida, K. *et al.* Spin Seebeck insulator. *Nat. Mater.* **9,** 894–897 (2010).
17. Demidov, V. E. *et al.* Magnetic nano-oscillator driven by pure spin current. *Nat. Mater.* **11,** 1028–1031 (2012).
18. Vlietstra, N. *et al.* Exchange magnetic field torques in YIG/Pt bilayers observed by the spin-Hall magnetoresistance. *Appl. Phys. Lett.* **103,** 032401 (2013).
19. Nakayama, H. *et al.* Spin Hall magnetoresistance induced by a nonequilibrium proximity effect. *Phys. Rev. Lett.* **110,** 206601 (2013).
20. Flipse, J. *et al.* Observation of the spin peltier effect for magnetic insulators. *Phys. Rev. Lett.* **113,** 027601 (2014).
21. Hamadeh, A. *et al.* Full control of the spin-wave damping in a magnetic insulator using spin-orbit torque. *Phys. Rev. Lett.* **113,** 197203 (2014).
22. Meyer, S. *et al.* Anomalous hall effect in YIG|Pt bilayers. *Appl. Phys. Lett.* **106,** 132402 (2015).
23. Onbasli, M. C. *et al.* Pulsed laser deposition of epitaxial yttrium iron garnet films with low Gilbert damping and bulk-like magnetization. *APL Mater.* **2,** 106102 (2014).
24. Chang, H. *et al.* Nanometer-thick yttrium iron garnet films with extremely low damping. *IEEE Magn. Lett.* **5,** 1–4 (2014).
25. Fan, Y. *et al.* Magnetization switching through giant spin–orbit torque in a magnetically doped topological insulator heterostructure. *Nat. Mater.* **13,** 699–704 (2014).
26. Rojas-Sánchez, J.-C. *et al.* Spin pumping and inverse spin Hall effect in platinum: the essential role of spin-memory loss at metallic interfaces. *Phys. Rev. Lett.* **112,** 106602 (2014).
27. Wang, Z., Sun, Y., Wu, M., Tiberkevich, V. & Slavin, A. Control of spin waves in a thin film ferromagnetic insulator through interfacial spin scattering. *Phys. Rev. Lett.* **107,** 146602 (2011).
28. Hahn, C. *et al.* Comparative measurements of inverse spin Hall effects and magnetoresistance in YIG/Pt and YIG/Ta. *Phys. Rev. B* **87,** 174417 (2013).
29. d'Allivy Kelly, O. *et al.* Inverse spin Hall effect in nanometer-thick yttrium iron garnet/Pt system. *Appl. Phys. Lett.* **103,** 082408 (2013).
30. Chiba, T., Bauer, G. E. W. & Takahashi, S. Current-induced spin torque resonance for magnetic insulators. *Physical Review Applied* **2,** 034003 (2014).
31. Iguchi, R., Sato, K., Hirobe, D., Daimon, S. & Saitoh, E. Effect of spin Hall magnetoresistance on spin pumping measurements in insulating magnet/metal systems. *Appl. Phys. Express* **7,** 013003 (2014).
32. Miao, B. F., Huang, S. Y., Qu, D. & Chien, C. L. Physical origins of the new magnetoresistance in Pt/YIG. *Phys. Rev. Lett.* **112,** 236601 (2014).
33. Wang, W. X. *et al.* Joule heating-induced coexisted spin Seebeck effect and spin Hall magnetoresistance in the platinum/Y3Fe5O12 structure. *Appl. Phys. Lett.* **105,** 182403 (2014).
34. Moog, E. R. & Bader, S. D. Smoke signals from ferromagnetic monolayers: p(1 × 1) Fe/Au(100). *Superlattices Microstruct.* **1,** 543–552 (1985).
35. Straub, M., Vollmer, R. & Kirschner, J. Surface magnetism of ultrathin γ-Fe films investigated by nonlinear magneto-optical Kerr effect. *Phys. Rev. Lett.* **77,** 743–746 (1996).
36. Rasing, T. Nonlinear magneto-optics. *J. Magn. Magn. Mater.* **175,** 35–50 (1997).
37. Qiu, Z. Q. & Bader, S. D. Surface magneto-optic Kerr effect. *Rev. Sci. Instrum.* **71,** 1243–1255 (2000).
38. Sih, V. *et al.* Spatial imaging of the spin Hall effect and current-induced polarization in two-dimensional electron gases. *Nat. Phys.* **1,** 31–35 (2005).
39. Stern, N. P., Steuerman, D. W., Mack, S., Gossard, A. C. & Awschalom, D. D. Drift and diffusion of spins generated by the spin Hall effect. *Appl. Phys. Lett.* **91,** 062109 (2007).
40. Kirilyuk, A., Kimel, A. V. & Rasing, T. Ultrafast optical manipulation of magnetic order. *Rev. Mod. Phys.* **82,** 2731–2784 (2010).
41. von Korff Schmising, C. *et al.* Imaging ultrafast demagnetization dynamics after a spatially localized optical excitation. *Phys. Rev. Lett.* **112,** 217203 (2014).
42. Fan, X. *et al.* Quantifying interface and bulk contributions to spin–orbit torque in magnetic bilayers. *Nat. Commun.* **5** (2014).
43. Erve, O. M. J. *et al.* Optical detection of spin Hall effect in metals. *Appl. Phys. Lett.* **104,** 172402 (2014).
44. Emori, S., Bauer, U., Woo, S. & Beach, G. S. D. Large voltage-induced modification of spin-orbit torques in Pt/Co/GdOx. *Appl. Phys. Lett.* **105,** 222401 (2014).
45. Postava, K. *et al.* Anisotropy of quadratic magneto-optic effects in reflection. *J. Appl. Phys.* **91,** 7293–7295 (2002).
46. Mewes, T., Nembach, H., Rickart, M. & Hillebrands, B. Separation of the first- and second-order contributions in magneto-optic Kerr effect magnetometry of epitaxial FeMn/NiFe bilayers. *J. Appl. Phys.* **95,** 5324–5329 (2004).
47. Hamrle, J. *et al.* Huge quadratic magneto-optical Kerr effect and magnetization reversal in the Co2FeSi Heusler compound. *J. Phys. Appl. Phys.* **40,** 1563–1569 (2007).
48. Lang, M. *et al.* Proximity induced high-temperature magnetic order in topological insulator—ferrimagnetic insulator heterostructure. *Nano Lett.* **14,** 3459–3465 (2014).
49. Althammer, M. *et al.* Quantitative study of the spin Hall magnetoresistance in ferromagnetic insulator/normal metal hybrids. *Phys. Rev. B* **87,** 224401 (2013).
50. Lin, T., Tang, C., Alyahayaei, H. M. & Shi, J. Experimental investigation of the nature of the magnetoresistance effects in Pd-YIG hybrid structures. *Phys. Rev. Lett.* **113,** 037203 (2014).

51. Vlietstra, N. *et al.* Simultaneous detection of the spin-Hall magnetoresistance and the spin-Seebeck effect in platinum and tantalum on yttrium iron garnet. *Phys. Rev. B* **90,** 174436 (2014).
52. Hoffmann, A. Spin Hall effects in metals. *IEEE Trans. Magn.* **49,** 5172–5193 (2013).
53. Yu, G. *et al.* Magnetization switching through spin-Hall-effect-induced chiral domain wall propagation. *Phys. Rev. B* **89,** 104421 (2014).
54. Harder, M., Cao, Z. X., Gui, Y. S., Fan, X. L. & Hu, C.-M. Analysis of the line shape of electrically detected ferromagnetic resonance. *Phys. Rev. B* **84,** 054423 (2011).

Acknowledgements

Author contributions

M.M., P.U. and K.L.W. conceived the research; M.M. designed and performed the experiments and data analysis with contributions from P.U., P.K.A., R.N.S. and K.L.W.; M.M. and P.U. designed the theoretical model; M.C.O. grew the YIG film; G.Y. grew the Ta/CoFeB/MgO and Pt films; K.W. and M.L. fabricated the devices; M.M., P.U., P.K.A. and K.L.W. wrote the paper; all authors discussed the results and commented on the manuscript; the study was carried out under supervision of K.L.W.

Additional information

Supplementary Information accompanies this paper at http://www.nature.com/naturecommunications

Competing financial interests: The authors declare no competing financial interests.

Reprints and permission information is available online at http://npg.nature.com/reprintsandpermissions/

How to cite this article: Montazeri, M. *et al.* Magneto-optical investigation of spin–orbit torques in metallic and insulating magnetic heterostructures. *Nat. Commun.* 6:8958 doi: 10.1038/ncomms9958 (2015).